Ultrafast Nonequilibrium Enhancement of Electron-Phonon Interaction in 2 H – MoTe 2

Nina Girotto Erhardt, Sotirios Fragkos, Dominique Descamps, Stéphane Petit, Michael Schüler, Dino Novko, Samuel Beaulieu

Ultrafast Nonequilibrium Enhancement of Electron-Phonon Interaction in 2H-$MoTe_2$

Nina Girotto Erhardt,[1,2,*] Sotirios Fragkos,[3,*] Dominique Descamps,[3] Stéphane Petit,[3] Michael Schüler,[4,5] Dino Novko,[2,†] and Samuel Beaulieu[3,‡]

[1]European Theoretical Spectroscopy Facility, Institute of Condensed Matter and Nanosciences, Université catholique de Louvain, Chemin des Étoiles 8, B-1348, Louvain-la-Neuve, Belgium
[2]Centre for Advanced Laser Techniques, Institute of Physics, 10000 Zagreb, Croatia
[3]Université de Bordeaux—CNRS—CEA, CELIA, UMR5107, F33405 Talence, France
[4]PSI Center for Scientific Computing, Theory and Data, 5232 Villigen PSI, Switzerland
[5]Department of Physics, University of Fribourg, CH-1700 Fribourg, Switzerland

(Received 18 April 2025; revised 17 July 2025; accepted 15 August 2025; published 1 October 2025)

Understanding nonequilibrium electron-phonon interactions at the microscopic level and on ultrafast timescales is a central goal of modern condensed matter physics. Combining time- and angle-resolved extreme ultraviolet photoemission spectroscopy with constrained density functional perturbation theory, we demonstrate that photoexcited carrier density can serve as a tuning knob to enhance electron-phonon interactions in nonequilibrium conditions. Specifically, nonequilibrium band structure mapping and valley-resolved ultrafast population dynamics in semiconducting transition-metal dichalcogenide 2H-$MoTe_2$ reveal band-gap renormalizations and reduced population lifetimes as photoexcited carrier densities increase. Through theoretical analysis of photoinduced electron and phonon energy and linewidth renormalizations, we attribute these transient features to nonequilibrium modifications of electron-phonon coupling matrix elements. This Letter advances our understanding of microscopic coupling mechanisms enabling control over relaxation pathways in driven solids.

DOI: 10.1103/dvlz-93t8

Electron-phonon coupling (EPC) plays a fundamental role in shaping various material properties, including charge transport, thermal conductivity, optical responses, and phase transitions [1]. In transition-metal dichalcogenides (TMDCs), EPC is a key driver of charge-ordered states and superconductivity [2–7], where its influence is primarily dictated by the strength of the EPC matrix elements and their screening [2,8–10]. Notably, in multivalley semiconducting TMDCs, EPC exhibits an unconventional enhancement with increasing static equilibrium doping, attributed to the inefficient screening of strongly coupled out-of-plane phonon modes [11]. This behavior has significant implications for superconducting properties [6,7].

In nonequilibrium settings, ultrafast spectroscopic techniques are well suited to investigating EPC-related phenomena. While time-resolved optical spectroscopies allow for investigating energy and carrier relaxation processes [12,13], ultrafast electron diffraction tracks energy flow into and within the lattice degree of freedom in a momentum-resolved fashion [14–16]. Moreover, time- and angle-resolved photoemission spectroscopy provides an energy- and momentum-resolved view on nonequilibrium phenomena driven by EPC such as transient band renormalizations, nonequilibrium phase transitions, coherent phonons, and electronic population lifetimes [17]. In photoexcited solids, EPC is responsible for electron relaxation on multiple different timescales [18–20], anisotropic nonthermal phonon relaxation [21], and thermalization bottlenecks [22–24]. However, the microscopic mechanisms underlying photoinduced modifications of EPC remain poorly understood. For instance, experimental time-resolved studies of graphene demonstrated both an apparent enhancement [25] and a reduction [26] of EPC strength, depending on the excitation conditions. However, theoretical consensus on the origin of these modifications has not been reached [27,28]. A similar debate exists for photoexcited TMDCs. Indeed, a recent time-dependent density-functional-theory study showed that photoexcitation of MoS_2 enhances the EPC strength of optical phonons due to reduced electronic screening [29]. In contrast, femtosecond electron diffuse scattering and corresponding *ab initio* simulations of time-dependent Boltzmann equations (TDBEs) with additional carrier

*These authors contributed equally to this work.
†Contact author: dino.novko@gmail.com
‡Contact author: samuel.beaulieu@u-bordeaux.fr

screening found that photoexcitation reduces EPC of optical phonons, suppressing intravalley phonon-related scattering [30]. It is thus crucial to combine state-of-the-art experimental and theoretical techniques sensitive to both electron and lattice degrees of freedom to resolve the debate on microscopic mechanisms underlying photoinduced EPC modifications. This is particularly relevant for debated ultrafast light-induced EPC-related phenomena, such as photoinduced or quenched superconductivity [31,32] and structural order [33,34].

In this Letter, we present a joint experimental and theoretical study of nonequilibrium EPC in 2H-$MoTe_2$. Using time- and angle-resolved extreme ultraviolet (XUV) photoemission spectroscopy with a momentum microscope detection scheme, we track the evolution of the electronic structure and excited-state population dynamics in a valley-resolved manner as a function of the photoexcited carrier density. By correlating these measurements with constrained density functional perturbation theory (cDFPT), providing nonthermal momentum-resolved renormalizations of phonons [28,35,36], we directly link the experimentally observed band-gap renormalizations and carrier lifetime reductions to photoinduced modifications of EPC matrix elements. This Letter highlights the critical role of EPC and the corresponding screening effects arising from photoinduced carrier distribution in TMDCs—an essential feature that is often overlooked in conventional thermalization theories, including effective temperature models and TDBEs [37,38].

The experimental setup [Fig. 1(a)] is articulated around a polarization-tunable ultrafast XUV beamline [39] coupled with a momentum microscope apparatus [40,41]. More details can be found in Sec. S1 of the Supplemental Material (SM) [42], as well as in Ref. [53]. Figure 1(b) presents a schematic illustrating the equilibrium (left) and photoinduced screened nonequilibrium EPC (right), emphasizing the relative coupling strength (g^2) with acoustic and optical phonon branches. In Fig. 1(c), we show the static and nonequilibrium band structure mapping of 2H-$MoTe_2$ along the K-Σ-Γ high-symmetry direction, obtained with XUV pulses only (left panel) and at the temporal overlap between the IR and XUV pulses (right panel). Section S2 of the SM contains an extended discussion about these band position fitting procedures [42].

In TMDCs, where Coulomb potential is poorly screened and where strong many-body interactions are present, electron-hole pairs from optical excitation enhance Coulomb screening and modify EPC, leading to band-gap renormalization in nonequilibrium settings [54–56]. The investigation of photoexcited carrier density-dependent band-gap renormalizations thus provides valuable information about many-body effects determining the optical and electronic properties of TMDCs. Data presented in Fig. 2(b) reveal a direct band gap of $\Delta_g^d = 1.19 \pm 0.01$ eV at the K

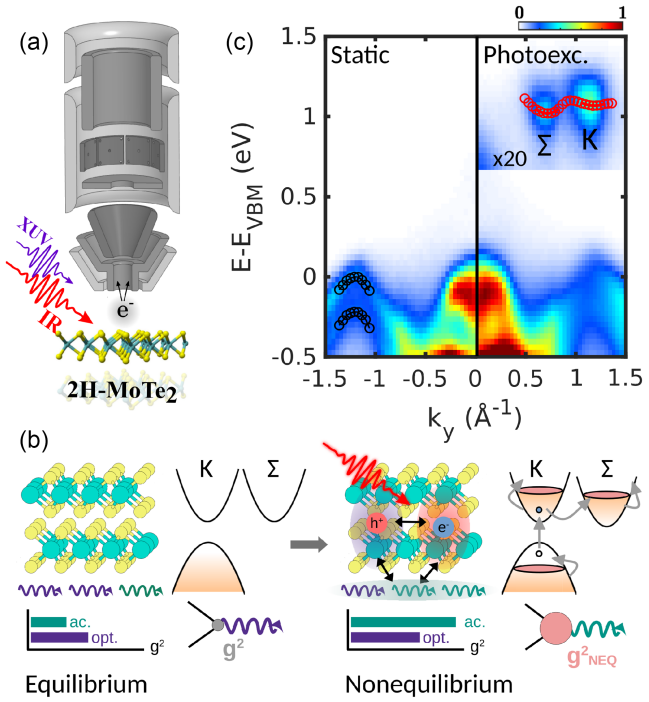

FIG. 1. Nonequilibrium band structure mapping and EPC in 2H-$MoTe_2$. (a) Infrared pump (1.2 eV, 135 fs) and XUV probe (21.6 eV) pulses are focused on a bulk 2H-$MoTe_2$ sample in the interaction chamber of a time-of-flight momentum microscope, at an incidence angle of 65° and with the light incidence plane along the crystal mirror plane (the Γ-M direction). (b) Schematic of the equilibrium (left) and nonequilibrium (right) EPC showing the relative coupling strength (g^2), with acoustic and optical phonon branches in both scenarios. (c) Static (left) and photoexcited energy-momentum cuts (at pump-probe overlap; right) along the Γ-Σ-K high-symmetry direction, recorded using s-polarized IR pump and p-polarized XUV probe pulses.

valley and an indirect band gap of $\Delta_g^i = 1.14 \pm 0.01$ eV at the Σ valley (for the lowest investigated photoexcited carrier density: 2.7×10^{13} cm^{-2}). When the photoexcited carrier density is increased from 2.7×10^{13} cm^{-2} (corresponding to a fluence of 0.9 mJ/cm^2) to 7.8×10^{13} cm^{-2} (corresponding to a fluence of 2.7 mJ/cm^2), both Δ_g^d and Δ_g^i monotonically decrease by a few tens of meV.

Beyond band-gap renormalization, the density of photoexcited electron-hole pairs can significantly influence the ultrafast relaxation mechanisms that govern the nonequilibrium behavior of materials. We thus turn our attention to the investigation of ultrafast valley-resolved electron dynamics in photoexcited 2H-$MoTe_2$ as a function of photoexcited carrier density. Integrating photoemission intensities in the conduction band for six K and Σ valleys [Fig. 3(a)] as a function of pump-probe delay yields the valley-resolved population dynamics shown in Fig. 3(b), here exemplified for the lowest (2.7×10^{13} cm^{-2}) and highest (7.8×10^{13} cm^{-2}) investigated photoexcited carrier densities. At our pump photon energy (1.2 eV), the only

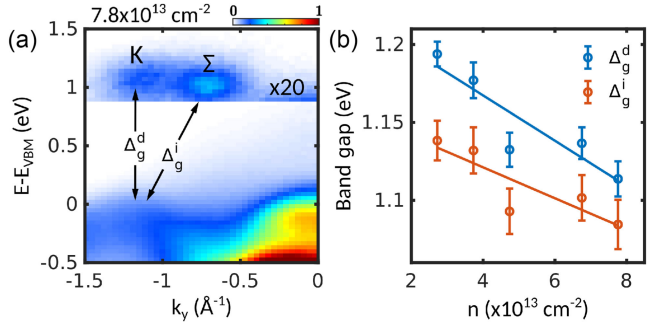

FIG. 2. Photoexcited carrier density-dependent direct and indirect band-gap renormalizations. (a) Energy-momentum cut along the K-Σ-Γ high-symmetry direction, at pump-probe temporal overlap, using s-polarized IR pump and p-polarized XUV probe pulses, with arrows showing the direct (Δ_g^d) and indirect (Δ_g^i) band gaps. (b) Photoexcited carrier density-dependent direct and indirect band-gap values.

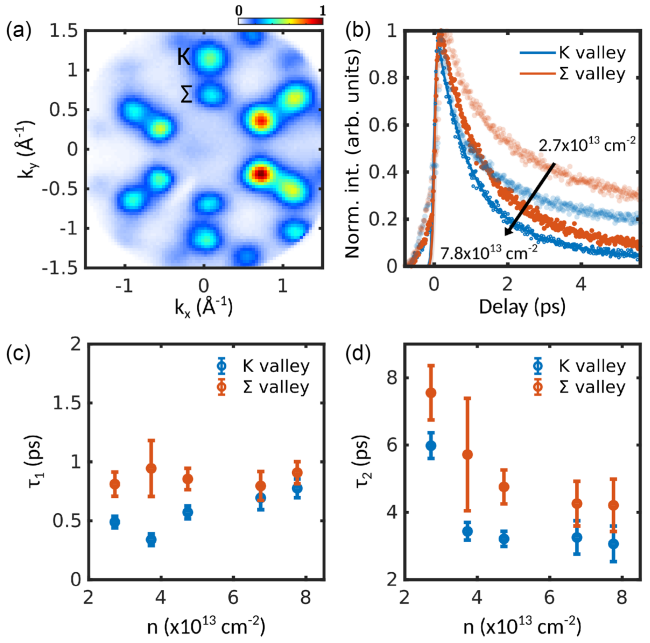

FIG. 3. Photoexcited carrier density-dependent valley-resolved population lifetimes (a) Constant energy contour of excited states near the conduction band minima at the K and Σ valleys. The forward-backward asymmetry in photoemission intensity arises from the photoemission transition dipole matrix elements. (b) Time-resolved population dynamics in the K (blue) and Σ (red) conduction band valleys for two photoexcited carrier densities (2.7×10^{13} cm^{-2} and 7.8×10^{13} cm^{-2}). (c),(d) Valley-resolved photoexcited carrier density-dependent time constants (τ_1 and τ_2, respectively).

accessible bright optical transition is located around the BZ boundary (the K valleys). Following photoexcitation at the K valleys, carriers undergo ultrafast intervalley scattering to the Σ global conduction band minima, as reported in similar semiconducting 2H-TMDCs [57–60]. The population dynamics at the K and Σ valleys can be fitted by a double-exponential decay function multiplied by a sigmoid function that accounts for initial photoexcitation using an IR pump with a finite duration (see Sec. S3 of the SM [42]). In Figs. 3(c) and 3(d), we report the extracted valley-resolved and photoexcited carrier density-dependent fast (τ_1) and slow (τ_2) time constants associated with the fitted double-exponential decays.

Figure 3(c) reveals that the fast time constant (τ_1) in the Σ valleys appears to be largely independent of photoexcited carrier density, remaining slightly below 1 ps. However, the dynamics in the K valleys exhibit a different trend. Indeed, we observe a global increase in lifetime with carrier densities (with a small deviation from this trend at low density). This behavior at the K valley can be reasonably attributed to the hot phonon bottleneck effect [20,22,61,62] (see Secs. S4 and S5 of the SM [42]). Strikingly, the slower time constant (τ_2) exhibits a strong and opposite photoexcited carrier density dependence [Fig. 3(d)]. Indeed, population lifetimes at both the K and Σ valleys become significantly shorter as photoexcited carrier density increases. While these results demonstrate the possibility of tailoring ultrafast population lifetimes using different excitation conditions, which have also been discussed in previous studies [28–30], the microscopic origin behind these renormalized nonequilibrium scattering processes has been subject to debate.

Indeed, such phenomena are often discussed in the context of modified scattering phase space versus photo-induced alteration of EPC matrix elements [3,26–29]. In the case of TMDCs, a recent ultrafast electron diffraction study suggested that modifications to the EPC matrix elements do not play a decisive role for $TiSe_2$ [3], while a few experimental and theoretical surveys reported significant modifications (both increases and decreases) in screening of EPC in photoexcited MoS_2 [29,30]. To resolve the debate about the microscopic origin of this nonequilibrium tuning knob of EPC, we performed state-of-the-art cDFPT calculations [28].

By performing first-principles density-functional-theory calculations on a 2H-$MoTe_2$ bilayer, the conduction band minima are located at Σ high-symmetry points, in agreement with experimental measurements [Fig. 4(a)]. To analyze the linewidths, scattering rates, and carrier lifetimes, we computed the electron spectral function, which incorporates the Fan-Migdal electron self-energy arising from EPC [1]. The self-energy is computed from many-body perturbation theory (MBPT) using either unscreened EPC matrix elements from DFPT [63] or screened EPC matrix elements from cDFPT. Therefore, combining MBPT with cDFPT captures both the effect of modified scattering phase space and a renormalized EPC matrix element in nonequilibrium conditions, while a combination with DFPT includes only the former.

In Fig. 4(a), we show the band-projected conduction electron linewidth ($\gamma_{n\mathbf{k}}$) due to electron-phonon scattering using the equilibrium DFPT approach (see the SM for

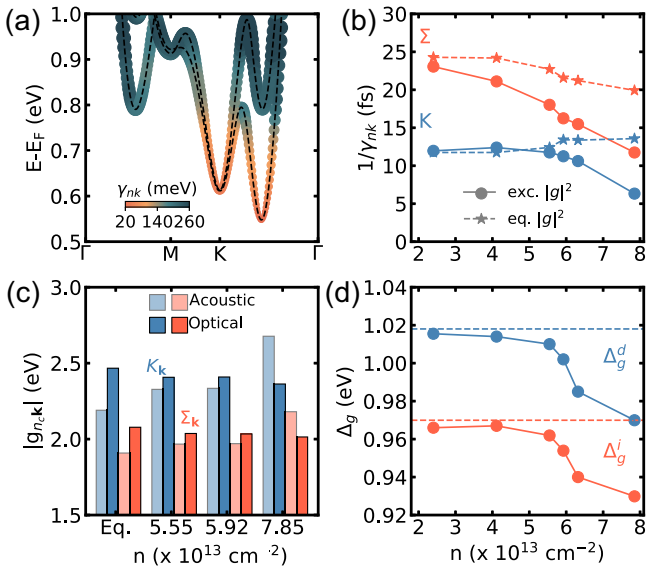

FIG. 4. Equilibrium and nonequilibrium electronic properties of bilayer 2H-$MoTe_2$. (a) Band-projected electron linewidth (γ_{nk}) for conduction bands of bilayer 2H-$MoTe_2$ along the Γ-M-K-Γ path. (b) Single-particle electron lifetimes ($1/\gamma_{nk}$) for various photoexcited carrier densities. The stars and dashed lines represent results obtained using equilibrium EPC matrix elements (eq. $|g|^2$), while the filled circles and full lines show results of cDFPT calculations (including screening of EPC matrix elements by photoexcited carriers, exc. $|g|^2$). (c) Equilibrium and nonequilibrium EPC matrix elements ($|g_{q,\nu}|$) at the bottom of the K (blue) and Σ (red) valleys, separated in their acoustic (faint colors) and optical (bold colors) phonon contributions. (d) Direct (Δ_g^d, blue) and indirect (Δ_g^i, red) band gaps as a function of photoexcited carrier density. The dashed horizontal lines represent the associated band-gap values for which no photoexcited carrier screening of $|g|^2$ is considered.

computational details [42]), which exhibits a monotonic increase of linewidth with energy. This behavior is quite general [64–66] and persists in nonequilibrium settings [58,67]. The inverse of electron linewidth ($1/\gamma_{n\mathbf{k}}$) corresponds to single-particle lifetimes. In Fig. 4(b), we show how single-particle lifetime decreases as a photoexcited carrier density increases in both the K and Σ valleys. This effect is entirely due to a change in EPC matrix elements, as shown in Fig. 4(c) (see also Fig. S3 in the SM [42]). The linewidth calculation with equilibrium EPC matrix elements [the dashed line in Fig. 4(d)] misses out on the decreasing trend of the electron lifetime. Visible consequences of the photoinduced change in the EPC matrix elements occur in the larger carrier concentration regime. For the lower concentrations, the experimentally observed decrease of τ_2 might be attributed to electron-electron scattering [68]. In the EPC regime, we evaluate $|g_{n_c\mathbf{k}}| = \sum_{\mathbf{q}\nu m} |g_{\nu n_c m}(\mathbf{k},\mathbf{q})|$ for a fixed $\mathbf{k}$ and the first conduction band (n_c) and observe that, for both valleys ($\mathbf{k} = \mathrm{K}, \Sigma$), coupling of the first conduction band to acoustic phonons strengthens upon photoexcitation, while coupling to the optical modes weakens. In addition, consistent with experimental observations, EPC is stronger (shorter lifetime) at the K valley (compared to Σ). However, single-particle lifetimes are 2 orders of magnitude smaller than the experimentally measured population lifetimes. This behavior is expected, considering that the latter reflects the collective two-particle scattering process [69], where the scattering rate is additionally reduced by electron-hole interaction (vertex correction). Nevertheless, the observed trend in photoexcited carrier density-dependent lifetimes is not affected by this additional process [69]. Also, it was shown that Boltzmann equations overestimate (underestimate) the scattering rate (lifetime) for stronger interactions and are far from equilibrium [70]. Moreover, as seen experimentally, we observe photoinduced direct (Δ_g^d) and indirect (Δ_g^i) band-gap shrinkage with increasing photoexcited carrier densities when properly accounting for renormalization of EPC matrix elements in nonequilibrium conditions. The impact of dynamical modification of EPC on band-gap shrinkage is evident when comparing results obtained using screened (round markers and solid lines; cDFPT) and unscreened (dashed lines; DFPT) EPC matrix elements in Fig. 4(d). The weak band-gap renormalization for the lower carrier excitation ($< 4 \times 10^{13}$ cm^{-2}) might be enhanced by the inclusion of the electron-electron scattering effects [71]. Similarly, the overall underestimation of the absolute band gap (by around 0.15 eV) could be improved by accounting for the nonlocal electron correlations as in the GW approach [71].

To further distinguish between the effects coming from nonequilibrium modifications of the available electronic scattering phase space and EPC matrix elements, we computed the phonon spectral function $B_\nu(\mathbf{q},\omega)$ [via the phonon self-energy $\pi_\nu \propto |g_{q\nu}|^2 \chi_0(\mathbf{q},\omega)$, where $\chi_0(\mathbf{q},\omega)$ is the electronic susceptibility—see Sec. S6 of the SM for more details [42]] using two different approaches: (i) the DFPT approach, where we use equilibrium unscreened $|g_{q\nu}|^2$ and nonequilibrium screened $\chi_0(\mathbf{q},\omega)$ and (ii) the cDFPT approach, where both $|g_{q\nu}|^2$ and $\chi_0(\mathbf{q},\omega)$ are screened by the photoexcited nonequilibrium electron distribution. Comparing DFPT and cDFPT results allows us to analyze the nonequilibrium renormalization of EPC matrix elements [$\Delta|g_{q,\nu}|$; Fig. 5(c)], as well as its impact on the renormalization of the spectral function [$\Delta B_\nu(\mathbf{q},\omega)$; Fig. 5(b)]. In the differential spectral function map [$\Delta B_\nu(\mathbf{q},\omega)$; Fig. 5(b)], the negative (blue) differential signal is thus associated with enhanced spectral function using a DFPT approach, therefore capturing the role of photoexcited phase space for electronic transitions, while the positive (red) differential signal originates from an enhanced spectral function calculated using a cDFPT approach, thus yielding information about the dynamical renormalization of the EPC matrix elements.

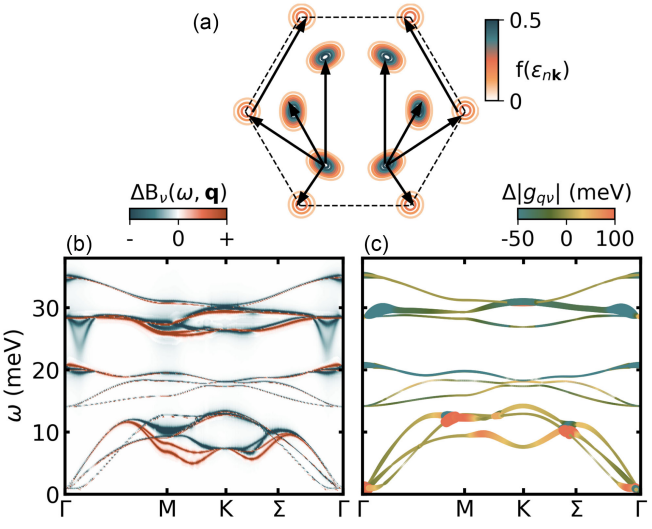

FIG. 5. Nonequilibrium phonon softening and renormalization of EPC matrix elements. (a) Electron occupation factors projected onto constant energy contours near conduction band minima. Arrows represent intervalley scattering processes, which are responsible for phonon softening. (b) Energy- and momentum-resolved nonequilibrium renormalization of the phonon spectral function $[\Delta B_\nu(\omega, \mathbf{q})]$. $\Delta B_\nu(\omega, \mathbf{q})$ is obtained by taking the difference between the phonon spectral function with equilibrium matrix elements and the phonon spectral function with nonequilibrium matrix elements. (c) Energy- and momentum-resolved nonequilibrium renormalization of EPC matrix elements $(\Delta|g_{q,\nu}|)$. $\Delta|g_{q,\nu}|$ is obtained by taking the difference between equilibrium and nonequilibrium EPC matrix elements and is projected onto the equilibrium phonon bands.

In Fig. 5(b), the primary effect of nonequilibrium phase-space modifications is the softening of strongly coupled long-wavelength optical phonon modes (the blue negative signal below 30 meV near Γ). Conversely, the dominant spectral function renormalization driven by modifications in the EPC matrix elements appears in the acoustic phonons near the M and Σ high-symmetry points (the red positive signal below 10 meV). The nonequilibrium decrease in EPC strength around the Brillouin zone center (mainly optical phonons), along with its enhancement near the Brillouin zone edge (mainly acoustic phonons), is further confirmed by the explicit subtraction of the non-equilibrium screened from the equilibrium screened $|g_{q\nu}|^2$ [see Fig. 5(c)]. Upon photoexcitation, the reduction in EPC strength for optical phonons is compensated for by a significant increase in coupling for acoustic modes, leading to an overall nonequilibrium enhancement of the EPC strength. This mechanism underlies the observed band-gap renormalization and shorter lifetimes with increasing photodoping, as seen in experiments.

In equilibrium, strong coupling to optical phonon branches near Γ is a known property of undoped TMDCs [11]. Moreover, in some cases, static carrier doping can promote coupling to the acoustic phonons [72,73], their subsequent softening, and the occurrence of dynamical instabilities [4,74,75]. Here, we observe a similar behavior for the case of nonequilibrium photodoping. Indeed, the increase of EPC matrix elements $(\Delta|g_{q\nu}|)$ for acoustic phonon modes (near 10 meV) around the M and Σ points [Fig. 5(c) and Sec. S4 of the SM [42]] and their subsequent softening and heating highlight their important role in the nonequilibrium electron-phonon physics of photoexcited 2H-$MoTe_2$. Similar observations were reported in time-resolved electron diffraction studies of 2H-WSe_2 [76] and 2H-$MoTe_2$ [77], where a significant buildup of phonon population at the M and Σ points was observed.

The effects of screening were also investigated from first principles in semiconducting 2H-$MoTe_2$ and were found to be crucial for describing the increase of ultrafast electron diffuse scattering signals at the K, M, and Σ points [78] and the reduction of the main Bragg peaks' intensity [30]. We not only confirmed a screening-induced reduction of EPC strengths for long-wavelength optical phonons [30] but also found significant photoinduced renormalization of the acoustic and optical mode coupling at finite $\mathbf{q}$ high-symmetry points (see also Fig. S3 of the SM [42]), leading to the increase of the total EPC strength (see Fig. S4 of the SM [42]) exemplified in the measured transient band gap and carrier lifetime decrease. We claim that photodoping, like conventional doping in TMDCs [11], is responsible for the redistribution of EPC matrix elements and is crucial to take into account in an *ab initio* self-consistent and fully momentum-resolved manner when describing carrier relaxation and phonon dynamics.

In conclusion, we have demonstrated that excitation density plays a critical role in enhancing EPC in photoexcited 2H-$MoTe_2$. By combining time- and angle-resolved XUV photoemission spectroscopy with cDFPT, we provided direct evidence of band-gap renormalizations and modified carrier lifetimes as a function of photoexcited carrier density. Our results reveal that increasing carrier densities enhances electron-phonon scattering rates, leading to a pronounced renormalization of phonon energies and linewidths. This effect is driven by modifications of EPC matrix elements, as confirmed by our theoretical calculations. Our results thus resolve the debate over the dominant microscopic mechanism governing ultrafast electron-phonon dynamics (modified scattering phase space versus photoinduced alteration of EPC matrix elements) in photoexcited semiconducting TMDCs.

Acknowledgments—We thank Nikita Fedorov, Romain Delos, Pierre Hericourt, Rodrigue Bouillaud, Laurent Merzeau, Frank Blais, and Yiming Pan for the technical assistance. S. B. gratefully acknowledges Yann Mairesse and Baptiste Fabre for the insightful and stimulating discussions. M. S. acknowledges support from SNSF Ambizione Grant No. PZ00P2-193527. We acknowledge

the financial support of the IdEx University of Bordeaux/ Grand Research Program "GPR LIGHT." We acknowledge support from ERC Starting Grant ERC-2022-STG No. 101076639, Quantum Matter Bordeaux, AAP CNRS Tremplin, and AAP SMR from Université de Bordeaux. S. F. acknowledges funding from the European Union's Horizon Europe research and innovation program under Marie Skłodowska-Curie 2024 Postdoctoral Fellowship No. 101198277 (TopQMat). N. G. E. and D. N. acknowledge financial support from the project "Podizanje znanstvene izvrsnosti Centra za napredne laserske tehnike (CALTboost)," financed by the European Union through the National Recovery and Resilience Plan 2021–2026 (NRPP). This work was supported by the Fonds de la Recherche Scientifique—FNRS under Grants No. T.0183.23 (PDR) and No. T.W011.23 (PDR-WEAVE). Computational resources have been provided by the Consortium des Équipements de Calcul Intensif (CÉCI), funded by the FRS-FNRS under Grant No. 2.5020.11.

The views and opinions expressed herein do not necessarily reflect those of the European Commission. Neither the European Union nor the granting authority can be held responsible for them.

Data availability—The data that support the findings of this Letter are openly available [79].

[1] F. Giustino, Rev. Mod. Phys. **89**, 015003 (2017).
[2] X. Zhu, Y. Cao, J. Zhang, E. W. Plummer, and J. Guo, Proc. Natl. Acad. Sci. U.S.A. **112**, 2367 (2015).
[3] M. R. Otto, J.-H. Pöhls, L. P. R. de Cotret, M. J. Stern, M. Sutton, and B. J. Siwick, Sci. Adv. **7**, eabf2810 (2021).
[4] M. K. Bin Subhan, A. Suleman, G. Moore, P. Phu, M. Hoesch, H. Kurebayashi, C. A. Howard, and S. R. Schofield, Nano Lett. **21**, 5516 (2021).
[5] M. Kang, S. W. Jung, W. Shin, Y. Sohn, S. H. Ryu, T. Kim, M. Hoesch, and K. Kim, Nat. Mater. **17**, 676 (2018).
[6] S. W. Jung, M. D. Watson, S. Mukherjee, D. V. Evtushinsky, C. Cacho, E. Martino, H. Berger, and T. K. Kim, ACS Nano **18**, 33359 (2024).
[7] D. Costanzo, S. Jo, H. Berger, and A. F. Morpurgo, Nat. Nanotechnol. **11 4**, 339 (2015).
[8] F. Weber, S. Rosenkranz, J.-P. Castellan, R. Osborn, R. Hott, R. Heid, K.-P. Bohnen, T. Egami, A. H. Said, and D. Reznik, Phys. Rev. Lett. **107**, 107403 (2011).
[9] C. M. Varma and W. Weber, Phys. Rev. Lett. **39**, 1094 (1977).
[10] F. Weber, R. Hott, R. Heid, L. L. Lev, M. Caputo, T. Schmitt, and V. N. Strocov, Phys. Rev. B **97**, 235122 (2018).
[11] T. Sohier, E. Ponomarev, M. Gibertini, H. Berger, N. Marzari, N. Ubrig, and A. F. Morpurgo, Phys. Rev. X **9**, 031019 (2019).
[12] Z. Chi, H. Chen, Q. Zhao, and Y.-X. Weng, J. Chem. Phys. **151**, 114704 (2019).
[13] C. J. Sayers, A. Genco, C. Trovatello, S. D. Conte, V. O. Khaustov, J. Cervantes-Villanueva, D. Sangalli, A. Molina-Sanchez, C. Coletti, C. Gadermaier, and G. Cerullo, Nano Lett. **23**, 9235 (2023).
[14] R. P. Chatelain, V. R. Morrison, B. L. M. Klarenaar, and B. J. Siwick, Phys. Rev. Lett. **113**, 235502 (2014).
[15] H. Seiler, D. Zahn, M. Zacharias, P.-N. Hildebrandt, T. Vasileiadis, Y. W. Windsor, Y. Qi, C. Carbogno, C. Draxl, R. Ernstorfer, and F. Caruso, Nano Lett. **21**, 6171 (2021).
[16] T. Fukuda, U. Ozaki, S. Jeong, Y. Arashida, K. En-ya, S. Yoshida, P. J. Fons, J.-i. Fujita, K. Ueno, M. Hase, and M. Hada, J. Phys. Chem. C **127**, 13149 (2023).
[17] F. Boschini, M. Zonno, and A. Damascelli, Rev. Mod. Phys. **96**, 015003 (2024).
[18] T. P. H. Sidiropoulos, N. Di Palo, D. E. Rivas, S. Severino, M. Reduzzi, B. Nandy, B. Bauerhenne, S. Krylow, T. Vasileiadis, T. Danz, P. Elliott, S. Sharma, K. Dewhurst, C. Ropers, Y. Joly, M. E. Garcia, M. Wolf, R. Ernstorfer, and J. Biegert, Phys. Rev. X **11**, 041060 (2021).
[19] T. Kampfrath, L. Perfetti, F. Schapper, C. Frischkorn, and M. Wolf, Phys. Rev. Lett. **95**, 187403 (2005).
[20] E. Cappelluti, F. Caruso, and D. Novko, Prog. Surf. Sci. **97**, 100664 (2022).
[21] H. Seiler, D. Zahn, M. Zacharias, P.-N. Hildebrandt, T. Vasileiadis, Y. W. Windsor, Y. Qi, C. Carbogno, C. Draxl, R. Ernstorfer *et al.*, Nano Lett. **21**, 6171 (2021).
[22] L. Perfetti, P. A. Loukakos, M. Lisowski, U. Bovensiepen, H. Eisaki, and M. Wolf, Phys. Rev. Lett. **99**, 197001 (2007).
[23] J. C. Johannsen, S. Ulstrup, F. Cilento, A. Crepaldi, M. Zacchigna, C. Cacho, I. C. E. Turcu, E. Springate, F. Fromm, C. Raidel, T. Seyller, F. Parmigiani, M. Grioni, and P. Hofmann, Phys. Rev. Lett. **111**, 027403 (2013).
[24] D. Novko, F. Caruso, C. Draxl, and E. Cappelluti, Phys. Rev. Lett. **124**, 077001 (2020).
[25] E. Pomarico, M. Mitrano, H. Bromberger, M. A. Sentef, A. Al-Temimy, C. Coletti, A. Stöhr, S. Link, U. Starke, C. Cacho *et al.*, Phys. Rev. B **95**, 024304 (2017).
[26] K. Ishioka, M. Hase, M. Kitajima, L. Wirtz, A. Rubio, and H. Petek, Phys. Rev. B **77**, 121402(R) (2008).
[27] S.-Q. Hu, H. Zhao, C. Lian, X.-B. Liu, M.-X. Guan, and S. Meng, npj Quantum Mater. **7**, 14 (2022).
[28] N. Girotto and D. Novko, J. Phys. Chem. Lett. **14**, 8709 (2023).
[29] X.-B. Liu, S.-Q. Hu, D. Chen, M. Guan, Q. Chen, and S. Meng, Nano Lett. **22**, 4800 (2022).
[30] Y. Pan, P.-N. Hildebrandt, D. Zahn, M. Zacharias, Y. W. Windsor, R. Ernstorfer, F. Caruso, and H. Seiler, ACS Nano **19**, 11381 (2025).
[31] D. Fausti, R. I. Tobey, N. Dean, S. Kaiser, A. Dienst, M. C. Hoffmann, S. Pyon, T. Takayama, H. Takagi, and A. Cavalleri, Science **331**, 189 (2011).
[32] X. Zhang, Q. Liu, J.-W. Luo, A. J. Freeman, and A. Zunger, Nat. Phys. **10**, 387 (2014).
[33] T. Rohwer, S. Hellmann, M. Wiesenmayer, C. Sohrt, A. Stange, B. Slomski, A. Carr, Y. Liu, L. M. Avila, M. Kalläne *et al.*, Nature (London) **471**, 490 (2011).
[34] L. Stojchevska, I. Vaskivskyi, T. Mertelj, P. Kusar, D. Svetin, S. Brazovskii, and D. Mihailovic, Science **344**, 177 (2014).

[35] E. D. Murray, S. Fahy, D. Prendergast, T. Ogitsu, D. M. Fritz, and D. A. Reis, Phys. Rev. B **75**, 184301 (2007).

[36] K. Liu, S. Mao, S. Zhang, and J. Zhou, Nano Lett. **22**, 9006 (2022).

[37] L. Waldecker, R. Bertoni, R. Ernstorfer, and J. Vorberger, Phys. Rev. X **6**, 021003 (2016).

[38] F. Caruso and D. Novko, Adv. Phys. X **7**, 2095925 (2022).

[39] A. Comby, D. Rajak, D. Descamps, S. Petit, V. Blanchet, Y. Mairesse, J. Gaudin, and S. Beaulieu, J. Opt. **24**, 084003 (2022).

[40] O. Tkach and G. Schönhense, Ultramicroscopy **276**, 114167 (2025).

[41] O. Tkach *et al.*, arXiv:2401.10084.

[42] See Supplemental Material at http://link.aps.org/supplemental/10.1103/dvlz-93t8, which includes Refs. [43–52], for more details on the experimental setup, the determination of the direct and indirect band gaps, the valley-resolved fitting of the electron population lifetimes, and the hot phonon bottleneck effect, as well as additional details on the EPC matrix elements and computational details.

[43] R. P. Xian, Y. Acremann, S. Y. Agustsson, M. Dendzik, K. Bühlmann, D. Curcio, D. Kutnyakhov, F. Pressacco, M. Heber, S. Dong, T. Pincelli, J. Demsar, W. Wurth, P. Hofmann, M. Wolf, M. Scheidgen, L. Rettig, and R. Ernstorfer, Sci. Data **7**, 442 (2020).

[44] R. P. Xian, L. Rettig, and R. Ernstorfer, Ultramicroscopy **202**, 133 (2019).

[45] B. Munkhbat, P. Wróbel, T. J. Antosiewicz, and T. O. Shegai, ACS Photonics **9**, 2398 (2022).

[46] P. Giannozzi, O. Andreussi, T. Brumme, O. Bunau, M. B. Nardelli, M. Calandra, R. Car, C. Cavazzoni, D. Ceresoli, M. Cococcioni *et al.*, J. Phys. Condens. Matter **29**, 465901 (2017).

[47] A. A. Mostofi, J. R. Yates, Y.-S. Lee, I. Souza, D. Vanderbilt, and N. Marzari, Comput. Phys. Commun. **178**, 685 (2008).

[48] F. Giustino, M. L. Cohen, and S. G. Louie, Phys. Rev. B **76**, 165108 (2007).

[49] J. Noffsinger, F. Giustino, B. D. Malone, C.-H. Park, S. G. Louie, and M. L. Cohen, Comput. Phys. Commun. **181**, 2140 (2010).

[50] S. Poncé, E. Margine, C. Verdi, and F. Giustino, Comput. Phys. Commun. **209**, 116 (2016).

[51] M. J. van Setten, M. Giantomassi, E. Bousquet, M. J. Verstraete, D. R. Hamann, X. Gonze, and G. M. Rignanese, Comput. Phys. Commun. **226**, 39 (2018).

[52] N. Marzari, A. A. Mostofi, J. R. Yates, I. Souza, and D. Vanderbilt, Rev. Mod. Phys. **84**, 1419 (2012).

[53] S. Fragkos, Q. Courtade, O. Tkach, J. Gaudin, D. Descamps, G. Barrette, S. Petit, G. Schönhense, Y. Mairesse, and S. Beaulieu, arXiv:2507.02371.

[54] P. D. Cunningham, A. T. Hanbicki, K. M. McCreary, and B. T. Jonker, ACS Nano **11**, 12601 (2017).

[55] F. Liu, M. E. Ziffer, K. R. Hansen, J. Wang, and X. Zhu, Phys. Rev. Lett. **122**, 246803 (2019).

[56] L. Meckbach, J. Hader, U. Huttner, J. Neuhaus, J. T. Steiner, T. Stroucken, J. V. Moloney, and S. W. Koch, Phys. Rev. B **101**, 075401 (2020).

[57] R. Bertoni, C. W. Nicholson, L. Waldecker, H. Hübener, C. Monney, U. De Giovannini, M. Puppin, M. Hoesch, E. Springate, R. T. Chapman, C. Cacho, M. Wolf, A. Rubio, and R. Ernstorfer, Phys. Rev. Lett. **117**, 277201 (2016).

[58] P. Hein, A. Stange, K. Hanff, L. X. Yang, G. Rohde, K. Rossnagel, and M. Bauer, Phys. Rev. B **94**, 205406 (2016).

[59] R. Wallauer, J. Reimann, N. Armbrust, J. Güdde, and U. Höfer, Appl. Phys. Lett. **109**, 162102 (2016).

[60] S. Dong, M. Puppin, T. Pincelli, S. Beaulieu, D. Christiansen, H. Hübener, C. W. Nicholson, R. P. Xian, M. Dendzik, Y. Deng, Y. W. Windsor, M. Selig, E. Malic, A. Rubio, A. Knorr, M. Wolf, L. Rettig, and R. Ernstorfer, Nat. Sci. **1**, e10010 (2021).

[61] X. Shi, W. You, Y. Zhang, Z. Tao, P. M. Oppeneer, X. Wu, R. Thomale, K. Rossnagel, M. Bauer, H. Kapteyn, and M. Murnane, Sci. Adv. **5**, eaav4449 (2019).

[62] Z. Chi, H. Chen, Q. Zhao, and Y.-X. Weng, Nanotechnology **31**, 235712 (2020).

[63] S. Baroni, S. de Gironcoli, A. Dal Corso, and P. Giannozzi, Rev. Mod. Phys. **73**, 515 (2001).

[64] T. Valla, A. V. Fedorov, P. D. Johnson, and S. L. Hulbert, Phys. Rev. Lett. **83**, 2085 (1999).

[65] T. Valla, A. V. Fedorov, P. D. Johnson, J. Xue, K. E. Smith, and F. J. DiSalvo, Phys. Rev. Lett. **85**, 4759 (2000).

[66] M. Bernardi, D. Vigil-Fowler, J. Lischner, J. B. Neaton, and S. G. Louie, Phys. Rev. Lett. **112**, 257402 (2014).

[67] M. Düvel, M. Merboldt, J. P. Bange, H. Strauch, M. Stellbrink, K. Pierz, H. W. Schumacher, D. Momeni, D. Steil, G. S. M. Jansen, S. Steil, D. Novko, S. Mathias, and M. Reutzel, Nano Lett. **22**, 4897 (2022).

[68] M. Bauer, A. Marienfeld, and M. Aeschlimann, Prog. Surf. Sci. **90**, 319 (2015).

[69] S.-L. Yang, J. A. Sobota, D. Leuenberger, Y. He, M. Hashimoto, D. H. Lu, H. Eisaki, P. S. Kirchmann, and Z.-X. Shen, Phys. Rev. Lett. **114**, 247001 (2015).

[70] A. Picano, J. Li, and M. Eckstein, Phys. Rev. B **104**, 085108 (2021).

[71] A. Champagne, J. B. Haber, S. Pokawanvit, D. Y. Qiu, S. Biswas, H. A. Atwater, F. H. da Jornada, and J. B. Neaton, Nano Lett. **23**, 4274 (2023).

[72] X. Cui, H. Yan, X. Yan, K. Zhou, and Y. Cai, ACS Nano **17**, 16530 (2023).

[73] Y. Zhao, Z. Dai, C. Zhang, C. Lian, S. Zeng, G. Li, S. Meng, and J. Ni, New J. Phys. **20**, 043009 (2018).

[74] N. Girotto, F. Caruso, and D. Novko, J. Phys. Chem. C **127**, 16515 (2023).

[75] G. Marini and M. Calandra, Phys. Rev. Lett. **127**, 257401 (2021).

[76] L. Waldecker, R. Bertoni, H. Hübener, T. Brumme, T. Vasileiadis, D. Zahn, A. Rubio, and R. Ernstorfer, Phys. Rev. Lett. **119**, 036803 (2017).

[77] A. Krishnamoorthy *et al.*, Nano Lett. **19**, 4981 (2019).

[78] T. L. Britt, Q. Li, L. P. René de Cotret, N. Olsen, M. Otto, S. A. Hassan, M. Zacharias, F. Caruso, X. Zhu, and B. J. Siwick, Nano Lett. **22**, 4718 (2022).

[79] S. Beaulieu, N. Girotto Erhardt, S. Fragkos, D. Descamps, S. Petit, M. Schüler, and D. Novko, Ultrafast Nonequilibrium Enhancement of Electron-Phonon Interaction in 2H-$MoTe_2$ [Data set] (2025), 10.5281/zenodo.15791674.